

# On the origin of filamentary resistive switching in oxides-based memristive devices

R. Leal Martir<sup>1,2</sup>, E. A. Jagla<sup>2</sup>, D. Rubi<sup>3</sup>, and M. J. Sánchez<sup>1,2,\*</sup>

<sup>1</sup>*Instituto de Nanociencia y Nanotecnología (INN),*

*CONICET-CNEA, nodo Bariloche,*

*8400 San Carlos de Bariloche,*

*Río Negro, Argentina.*

<sup>2</sup>*Centro Atómico Bariloche,*

*Instituto Balseiro (UNCuyo), CONICET,*

*8400 San Carlos de Bariloche,*

*Río Negro, Argentina.*

<sup>3</sup>*Instituto de Nanociencia y Nanotecnología (INN),*

*CONICET-CNEA, nodo Buenos Aires, Argentina.*

(\*maria.sanchez@ib.edu.ar)

## Abstract

The control and manipulation of filamentary resistive switching (FRS) is essential for practical applications in fields like non-volatile memories and neuromorphic computing. However, key aspects of the dynamics of conductive filament formation and their influence on device resistance remain incompletely understood. In this work we study FRS in binary oxides based memristors by investigating the dynamics of oxygen vacancies (OV) on a two dimensional lattice and their role in forming low-resistance paths that facilitate the transition between high and low global resistance states. We reveal that the mere formation of an OV percolation path is insufficient to induce a transition to a low-resistance state. Instead, an OV concentration exceeding a critical threshold across all sites in the filament is required to generate a low-resistivity conducting path. Furthermore, we simulate the impact of static defects -which block OV migration and would correspond to voids in real porous samples-, on filament formation. We show that there is a range of defect density values where OV percolate through the sample, leading to the formation of OV filaments, but conductive paths remain absent. Additionally, a small concentration of defects can reduce the final value of the low-resistance state, thereby increasing the ON-OFF ratio. These findings provide valuable insights into optimizing defective nanomaterials with memristive properties, which are crucial for advancing in-memory and neuromorphic computing technologies.

## I. INTRODUCTION

Memristive devices are expected to be key components in the development of neuromorphic hardware [1, 2], intended to outperform current software-based algorithms by mimicking the structure and information processing mechanism of the brain [3, 4]. Typical devices are metal/insulator/metal (MIM) structures of micro-nanometer size that exhibit the resistive switching (RS) effect - i.e. the reversible change of the resistance upon the application of an electrical stimulus [5, 6].

Since almost two decades, numerous studies of RS in devices where the insulator is a transition metal oxide (TMO) -mainly binary compounds such as  $\text{TiO}_2$ ,  $\text{NiO}$ ,  $\text{HfO}_2$ ,  $\text{VO}_2$  and  $\text{Ta}_2\text{O}_5$ , among others[7–13]- have been reported as bipolar and attributed to the formation and retraction/rupture of nanoscale OV conducting filaments upon polarity reversal of the applied stimulus [14–18]. In binary TMO, it is well known that the local resistivity decreases with the OV content [19–21], and thus the formation/disruption of OV filaments seems to be at the origin of the resistive changes

[5, 22–24].

Although in situ detection and visualization of the precise location of conducting filaments are still challenging, filamentary RS has been experimentally characterized through various methodologies, including surface measurement techniques like conductive atomic force microscopy (c-AFM) and thermal mapping [7, 10, 25, 26], which reveal localized conduction paths. Additional insights have been gained through other imaging techniques such as scanning electron microscopy (SEM), and scanning transmission electron microscopy (STEM), which have provided direct evidence of conductive filaments [27–31]. Indirect metrics, such as the absence of scaling between resistance levels and device area, further corroborate the presence of filamentary structures [32].

In general, theoretical works on filamentary RS primarily focus on filament formation, either overlooking the underlying physical mechanisms [33–36] or presenting an incomplete picture of how these mechanisms impact the device’s overall resistance [37]. On the other hand, certain models such as the Voltage Enhanced OV migration (VEOV) model [38] have proven effective in reproducing the RS effect, by correlating the dynamics of OV with the different resistance states [8, 9, 39]. However, its one dimensional (1d) nature has precluded a thorough exploration of the role of localized defects that might be present in the sample which, as we will show, have a key impact on the formation and subsequent dynamics of filaments.

In order to overcome this limitation, the present study employs a two-dimensional (2d) resistor network model, in which the resistivities of the network depend on the OV concentration. The model, shortnamed OVRN (for Oxygen Vacancies Resistive Network), allows us to examine OV dynamics in a spatially resolved framework, providing new insights into how initial OV distributions, and its subsequent dynamics upon an external applied stimulus, determine the filament formation. In this way the OVRN captures the changes in the resistivities of the network, and the concomitant evolution of the resistance of the device. As we will show along the present work, inhomogeneities in the initial OV distribution are at the origin of conducting filament formation. In addition the duration of the applied electrical stimulus will be critical, affecting the filament size, width and stability. The OVRN model also opens the possibility to explore different types of localized defects such as grain boundaries [40–42] or porosity [43], and their role relevant to the RS effect- in particular the influence of such defects in the filamentary RS. A recent work by Xu et al. [37] studied the filament growth processes in electrochemical metallization cells employing kinetic Monte Carlo simulations, identifying three different growth modes and concluding that the density of high mobility regions is a relevant parameter to distinguish these modes. Our OVRN

model permits to define regions in the sample in which the OV concentration is maintained at zero, therefore producing an effect equivalent to that studied in [37]. However, we will make a key distinction between an OV filament (OVF) and a low resistivity conductive path (CP). With this distinction at hand we define two thresholds: one for OV percolation and the other for CP formation, which are identified and analyzed for different densities of localized defects. Furthermore, an interesting outcome of our study is a scaling effect in the temporal response of the resistance for different applied stimuli, that breaks down when the concentration of static defects exceeds a threshold.

## II. THE OVRN MODEL: OXYGEN VACANCIES DYNAMICS ON A 2D RESISTOR NETWORK

We start by introducing the OVRN model, which describes the resistivity change of a resistor network (RN) in terms of the migration of OV (positively charged) under an external electrical stimulus, making use of the well known dependence of the oxide's resistivity with the OV content. In this way, following the dynamics of OV profiles for an applied stimulus,  $V$ , we compute the changes in the resistance of the sample as a function of time.

The OVRN considers the sample as a rectangular array of  $N \times M$  nanodomains in the  $x - y$  plane, each one labelled by an index  $k$ ,  $1 \leq k \leq N \times M$ . The resistivity of each nanodomain  $\rho_k$ , is a function of the local OV concentration  $\delta_k$  (i.e., the number of OV in domain  $k$  divided by the total number of OV in the sample). This function is taken to be of the form

$$\rho_k = \rho_M - \rho_m \tanh[A(\delta_k - \delta_M)], \quad (1)$$

where  $\rho_m \equiv (H\rho - L\rho)/2$  and  $\rho_M \equiv (H\rho + L\rho)/2$ , are defined in terms of the minimum,  $L\rho$ , and maximum,  $H\rho$ , resistivities that a given domain can attain. The parameter  $\delta_M$  is an OV concentration threshold, such that for  $\delta_k = \delta_M$  the resistivity of the domain  $k$  is  $\rho_M$ . The sharpness of the transition between  $H\rho$  and  $L\rho$  is set by the parameter  $A$ . We notice that while more involved functional forms could be chosen, Eq.(1) nicely captures the behavior of binary TMOs, where OV act as n-type dopants supplying free electrons to the conduction band and thereby reducing the electrical resistance. We assume that the parameters  $\{\rho_m, \rho_M, \delta_M, A\}$  do not change among the different domains, which seems reasonable taking into account that we are modelling a simple capacitor-like geometry, with a single TMO in the MIM structure. We distinguish three main regions in the sample (Fig. 1a): the top and bottom interfaces TI and BI, (both defined as interfaces between the

top and bottom electrodes (TE, BE) with the TMO) and the central region C, which represents the bulk zone of the device. In addition, we define the active region (AR), which comprises the C and BI. Each domain  $k$  can allocate a concentration of OV,  $\delta_k$ , with an associated resistivity  $\rho_k(\delta_k)$ , and is identified as a node in the RN which has horizontal and vertical resistivities, both equal to  $\rho_k$ . This is equivalent to consider a diagonal resistivity tensor - a well justified assumption in the absence of magnetic field. Figure 1 b) displays the dependence of  $\rho_k$  on  $\delta_k$ , according to Eq.(1).

Given an external voltage  $V$  applied to the TE (the BE is grounded), we numerically solve the Kirchhoff's equations for the RN to obtain the horizontal and vertical potential drops at each domain  $\Delta V_{k,x}$  and  $\Delta V_{k,y}$ , and compute the total resistance of the array. Following Ref. 38, at each simulation step the OV profiles are updated according to

$$\delta_k(t + \Delta t) = \delta_k(t) + \sum_{k'} (p_{(k',k)} - p_{(k,k')}) \Delta t, \quad (2)$$

in terms of the probability rates given by

$$p_{(k,k'),l} = \delta_k(1 - \delta_{k'})e^{-V_\alpha + \Delta V_{k,l}}, \quad (3)$$

for OV transfer from a domain  $k$  to its four nearest neighbours  $k'$ , with  $l = x$ , or  $l = y$ . Note that the total amount of OV is fixed as vacancies are not permitted to escape the sample. The Arrhenius factor contains the local voltage drop  $\Delta V_{k,l}$  and the activation energy for OV diffusion  $V_\alpha$ , both in units of the thermal energy  $kT$ . The values of  $V_\alpha$  are the same along both directions  $x$  and  $y$ , assuming no specific anisotropies in the sample that could justify a different choice. Once the OV concentration at the step  $(t + \Delta t)$  is calculated,  $\rho_k(t + \Delta t)$  is obtained from Eq.(1) and the process starts again.

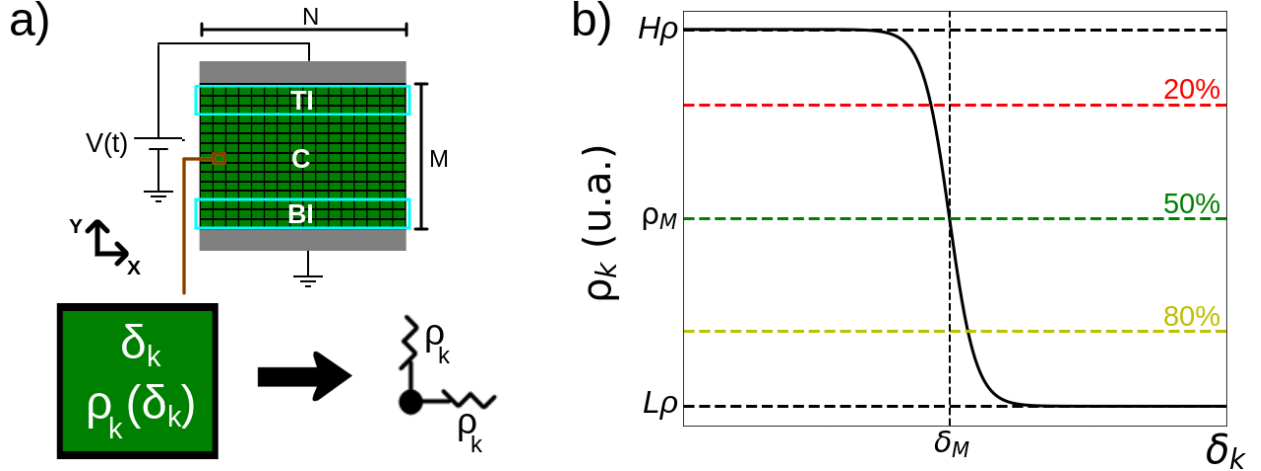


FIG. 1: (a) Sketch of the array of  $N \times M$  ( $N=60$ ,  $M=30$ ) nanodomains considered in the OVRN model. The TI, C and BI regions are highlighted. Each nanodomain  $k$  is identified with a site in the RN, with associated horizontal and vertical resistivities (both equal),  $\rho_k$ . (b) Resistivity of a nanodomain ( $k$ ) as a function of its OV concentration  $\delta_k$ . Three different resistivity threshold are shown and indicated by the coloured dashed lines. See text for more details.

The model incorporates the presence of  $n_O$  localized defects or static obstacles randomly distributed in the sample. These obstacles are considered to be places that OV cannot access. This is done by setting the OV concentration at the obstacles to be zero during the whole process. As we will discuss below, a key parameter that will determine the dynamics of OV filaments will be the density of obstacles,  $\nu_O = \frac{n_O}{N_T}$ , where  $N_T$  is the total number of domains.

### III. RESULTS

#### A. OV filaments, conductive paths and resistive changes in the absence of static defects

In this section we study the dynamics of OV for a given positive voltage  $V$ , in the absence of static defects /obstacles, i.e.  $\nu_O = 0$ . We take an initial OV profile concentrated on the TI, and obtained from a randomly generated gaussian-like distribution - see Fig.2 a). As in the OVRN we do not consider anisotropies in the parameters of the simulations, the anisotropy in the initial OV profile along the  $x$  direction acts as a “seed” for the formation of OV filaments, as we will discuss in the following. In this respect it can be mentioned that non-uniformities, like grain boundaries, are ubiquitous in amorphous or polycrystalline oxides- based films [44]. In addition, OV profiles

in equilibrium often exhibit a non-uniform distribution along the oxide [45].

Figure 2 b) shows the total resistance of the AR as a function of time (blue line). The black dots indicate the resistances at times t1 to t8 (in units of the simulation time) at which the OV and resistivities profiles depicted in Fig.2 c) were taken.

We define an OV filament (OVF) as a path connecting TI and BI, in which each site has an OV density  $\delta_k \geq 10^{-5}$ . This threshold can be slightly modified without affecting qualitatively our results. In addition a conductive path (CP) is defined as an OVF in which all the domains are in a low resistivity state, compared to some threshold (see below). From Eq.(1) it is clear that even after an OVF is formed, if  $\delta_k \ll \delta_M$  for some domains of the filament, the correspondent resistivities will be  $\rho_k \sim H_\rho$  and thus the OVF will not necessarily correspond to a path of low resistance- i.e. a CP. To be precise, to quantify “low resistivity” we employ three different thresholds, shown in Fig.1 c). The upper one is the 20% threshold, meaning that a domain with an OV concentration  $\delta_k$  has a ”low resistivity” if the condition  $L_\rho \leq \rho_k \leq H_\rho - 20\%(H_\rho - L_\rho)$  is satisfied. The same reasoning applies to the 50% and 80% thresholds.

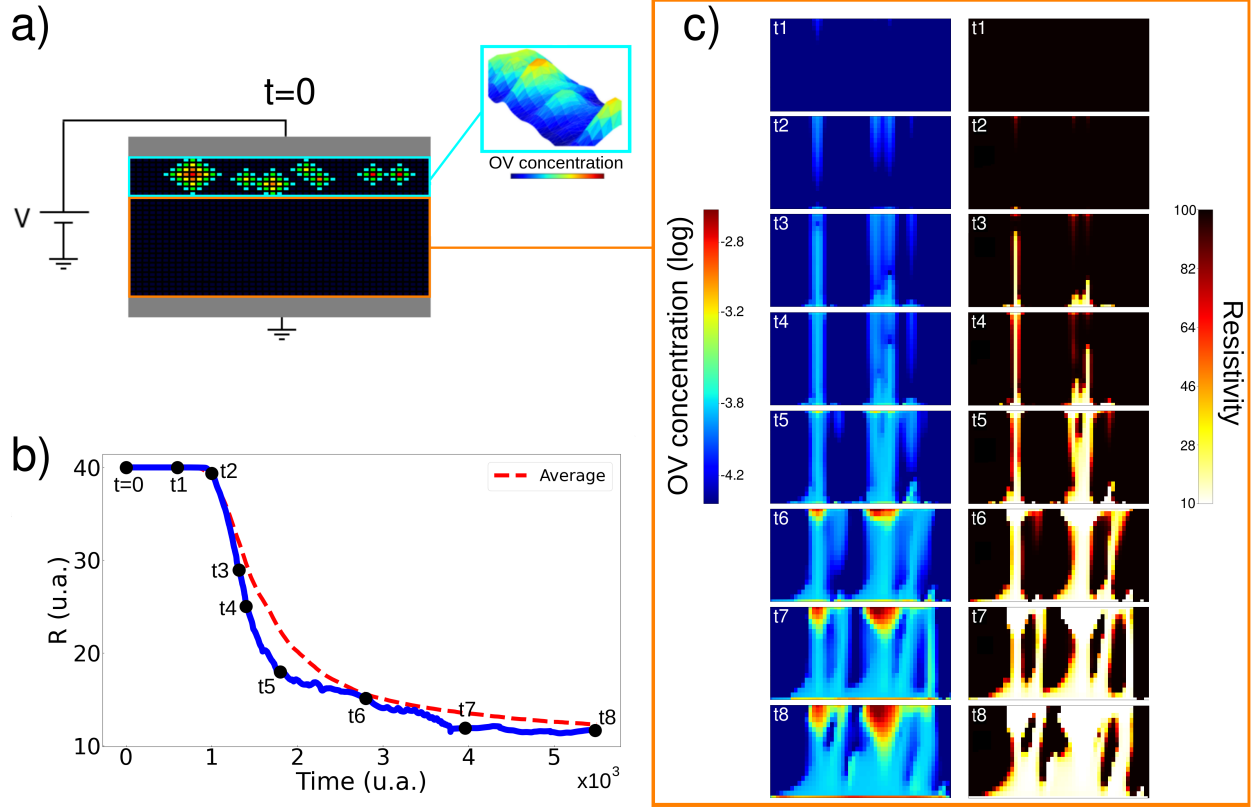


FIG. 2: (a) Sketch of the system at  $t = 0$ . Highlighted by squares are the TI (cyan) and AR (orange). The stimulus  $V$  starts at  $t = 0$  and is applied to the TE - the BE is grounded. The OV concentration's contour map and the 3D plot are also shown. (b) Resistance of the AR as a function of time. The average resistance, taken for a hundred of realizations is also shown (red dashed line). (c) OV (left) and resistivity (right) profiles along the AR, taken at different times  $t_1$  to  $t_8$  (shown in (b)). In all the cases the simulations were ran for  $\delta_M = 1.4 \cdot 10^{-4}$ ,  $A = 10^7$  and  $V = 250$  a.u. .

Different times,  $t_1$  to  $t_8$ , are chosen in order to characterize the stages in the formation of the OVFs and the CPs. For the smaller times,  $t_1$  and  $t_2$ , the OV concentration is still too low and no appreciable change in the resistance is obtained in Fig.2 b). Once one (or more than one) OVF is formed, OV start to accumulate at the BI (see Fig.2 c) for times  $t_3$  and  $t_4$ ) and therefore one (or more than one) CP starts to grow from the BI to the TI. This is concomitant with the sharp decrease in the resistance observed for times  $t_3$  to  $t_5$ . As long as the external stimulus is maintained, new OVFs and CPs can be formed, leading to a further resistance drop that can be seen for times  $t_6$  and  $t_7$ . Eventually, the resistance stabilizes as no new OVF or CP are formed, they only becoming thicker with time (see for example time  $t_8$ ).



The formation of metallic filaments in an environment where metallic ions, like Ag or Ta can move easily due to the absence of obstacles was also studied in electrochemical metallization cells (EMC) [37, 46–49]. However, we notice from our analysis that an OVF does not necessarily imply the formation of a CP, a fact that was disregarded in previous works. In our study, the CP is formed once the OV concentration overcomes a threshold value for all the domains of the OVF and it grows from the BI to the TI, i.e. in the opposite direction to the OVF growth. The present analysis can be easily extended to other realizations of the initial OV profile. As an example, in Fig.2 b) we plot (red dashed line) the average resistance calculated over a hundred of initial (gaussian-like) conditions of the OV profile, showing that it follows the same trend as the resistance curve corresponding to a single realization (blue curve). In addition we have checked that besides the random gaussian-like, other non uniform initial profiles can be employed in order to analyze the formation of OVFs.

An important issue to consider is the stability of the OVFs once the external stimulus is removed. Under this scenario, diffusive effects, ruled by the activation energy  $V_\alpha$ , start to dominate (see Eq.3) and could eventually lead to the OVF dissolution, a phenomenon that is relevant to characterize the volatility of the RS effect [50–52]. In order to analyze the OVF stability, we study the temporal evolution of the OVFs under an external voltage  $V$ , which is on during some time and subsequently removed. We focus on four OV concentration and resistivity profiles displayed in Fig.3 a) for times  $t_i$ , ( $i= 1, 4$ ), indicated in Fig.3 b). At time  $t_1$  the external stimulus is on, and it is switch off at time  $t_2$ , remaining off for the longer times  $t_3$  and  $t_4$ .

As it is shown in Fig.3 a), and in agreement with the previous analysis, two OVFs and CPs of different widths are formed between  $t_1$  and  $t_2$ - we denote the thicker CP by P1 and the thinner one by P2, respectively. Once the stimulus is removed, P2 dissolves while P1 remains formed but acquiring a hourglass-like shape [17, 50]. The fact that the thicker filament P1 remains formed has a clear effect on the overall resistance. In Fig.3 b) we plot the total resistance (upper panel) and the resistances (properly normalized to their respective maxima) of both P1 and P2 (bottom panel), as a function of time. Qualitatively, the total resistance follows the same behaviour as P1, indicating that the thicker CP dominates the trend in the overall resistance. In addition, as we already showed in Fig.2 c), OVF and CP widths can be controlled by the stimulus duration: longer stimulation leads to a lower resistance state, which is more resilient against diffusive effects [52].

To further elaborate on the idea of a dominant CP, in Fig.3 c) we plot, for a given realization and for a constant stimulus  $V=250$  a.u., the resistance of the OVF which once stabilized gives rise

to the dominant CP. In this case we can approximate the dominant OVF by a single 1d chain of nanodomains.

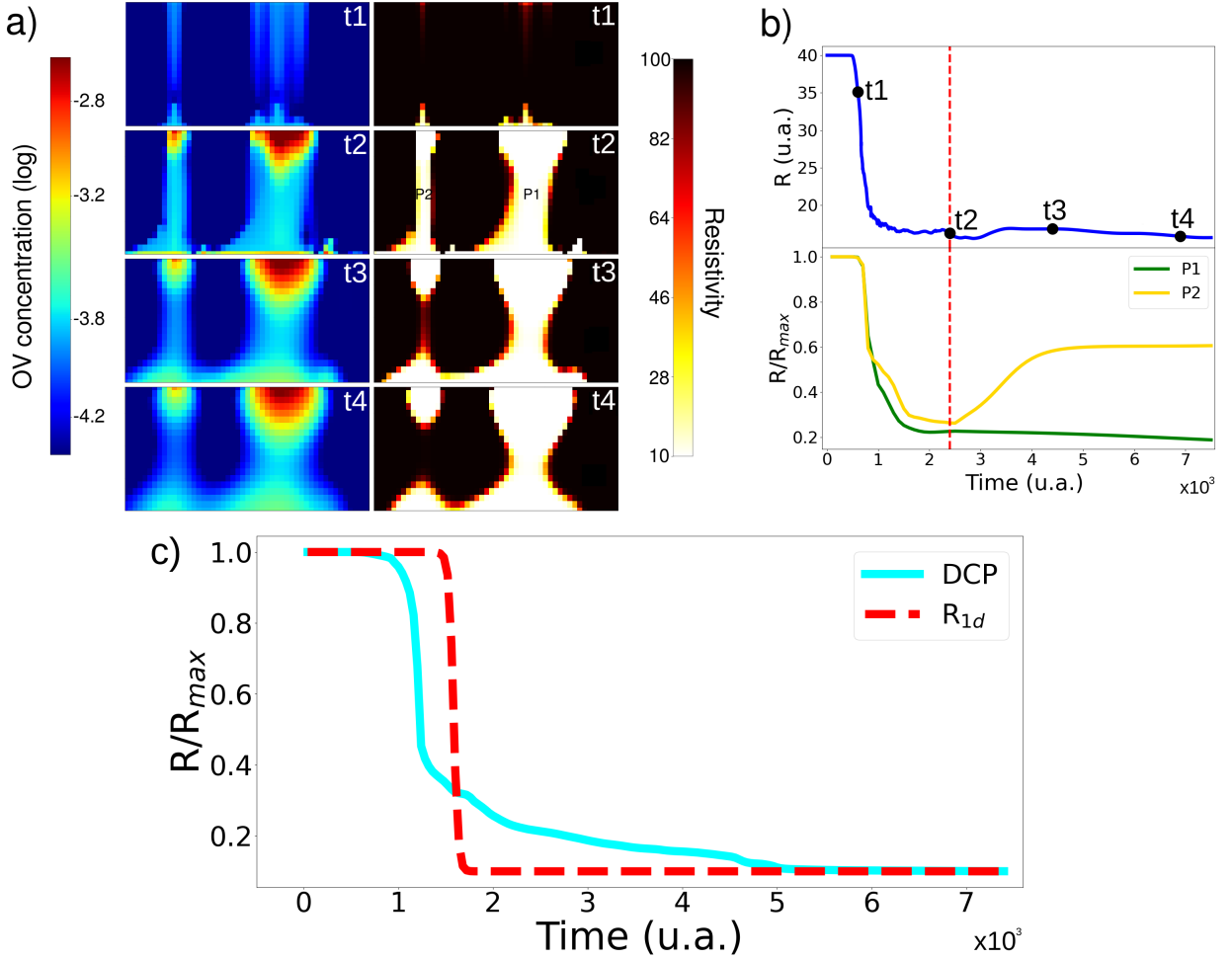


FIG. 3: (a) Evolution of OV distribution (left) and resistivity (right) profiles. At t1 the electrical stimulus ( $V=250$  a.u.) is on, and it is switched off at t2. Two CPs, P1 and P2, are identified. (b) Resistance of the AR (top) and of P1 and P2 (bottom), as a function of time. The resistances values at times t1 to t4 are highlighted by the black dots. The dashed vertical line highlight the time t2 when the stimulus is removed. (c) Normalized resistance as a function of time computed numerically for the dominant CP. Analytic calculation  $R_{1d}$  obtained from Eq.4 (red dashed line).

Assuming a CP of length  $L$  (and section  $S$ ), and for infinitesimally small domains, one can go to the continuous in the longitudinal dimension and compute the total resistance employing Eq.(1). After replacing  $\delta_i(t) \rightarrow \delta(x,t)$  for the OV profile at time  $t$ , and neglecting the geometric prefactor  $1/S$ , we get  $R_{1d}(t) = \int_0^L \rho(x,t) dx = \int_0^L (\rho_M - \rho_m \tanh[A(\delta(x,t) - \delta_M)]) dx$ .

The function  $\delta(x,t)$  does not have an analytic expression, so the above integral could only be

computed approximately by assuming a given functional form for the OV profile. The simplest, rather unjustified assumption, is to consider at each time an uniform profile across the CP:  $\delta(x, t) \equiv \delta_{unif}(t)$ . In this case it is obtained that

$$R_{1d}(t) = L\rho_M - L\rho_m \tanh[A(\delta_{unif}(t) - \delta_M)]. \quad (4)$$

To see how this analytic approximation works, we computed numerically for each simulation step the total OV concentration along the dominant OVF. After dividing it by the total number of sites of the OVF, we computed  $\delta_{unif}(t)$  and  $R_{1d}(t)$ , employing Eq. (4). The result is shown by the dashed line in Fig.3 c). Notice that the behaviour of the dominant CP resistance is quite well captured by  $R_{1d}(t)$ , particularly before and after the dominant filament is completely formed. For intermediate times, when the OVF is growing, the 1d model departs from the dominant CP resistance evolution, as the notion of a “dominant OVF” is only well defined once all the filaments have grown. Thus the uniform density approximation misses key information to properly capture the form of  $R(t)$  during the transient evolution. The 1d model also misses out diffusive effects - such as the OVF dissolution shown in Fig. 3a), and the influence of localized static defects, as we will analyze in the next section.

An interesting outcome of the previous analysis is the dependence of the temporal evolution of the resistance with the strength of the applied stimulus. In order to address this issue, we consider different applied voltages  $V_i$ , taking as initial OV concentration the gaussian-like profiles previously employed. Figure 4 a) (left panel) shows the resistance as a function of time for four different applied voltages (each curve is the average over a hundred realizations of the initial OV profile). In all the cases the initial resistance,  $R(t = 0) = R_H$  is the same. However, the resistance drop starts earlier in time and becomes more pronounced as the value of the voltage increases. In spite of this behaviour, all the resistance curves collapse onto a single one after a proper time scaling,  $\gamma_i t$ , with  $\gamma_i \equiv 1/\tau_i$  the inverse of a characteristic time,  $\tau_i$ , defined as the time the resistance remains on its initial (high) value for each voltage  $V_i$ . When plotting as a function of  $\gamma_i t$  all the curves are almost superimposed, as Fig.4 a) (right) shows. Notice that the collapse is extremely good till  $\gamma_i t \sim 2$  (see the black vertical dashed line in Fig.4 a) right panel). This is a confirmation of the initial exponential decay of the scaled resistance, as was also noticed by Tang et al. [53]. The scaling factors  $\gamma_i$  are shown in Fig. 4 b) for the four applied voltages (in a log-lin plot), showing a clear exponential dependence in consistency with the Arrhenius factor appearing in Eq.(3): the probability rate for OV migration increases exponentially with the applied voltage, which means

that for a given (constant)  $V_i$ , the time it takes the OV to reach the AR to generate the first resistance drop (as shown in Fig.2) decreases exponentially as  $V_i$  increases. As time further evolves, the resistance curves reach a minimum due to the fact that the OVFs and CPs are completely formed, in consistency with the results shown in Fig.2. Notice, however, that for longer times- and mainly due to lateral diffusion that tend to dissolve and eventually merge the already formed OVFs/CPs, a slight increase in the resistance is observed- as can be seen in Fig. 4 a) right panel. This effect is exemplified in Fig.4 c), where snapshots of the OV and resistivity profiles are shown for a single realization of the simulations (for  $V_3 = 250$  a.u.) and for (dimensionless) times  $\tau k \equiv \gamma_3 t k$ ,  $k = 1, 2, 3$  defined for  $\gamma_3$  and indicated in Fig. 4 a) right panel. At time  $\tau 1$  one identifies two completely formed CPs, in agreement with the minimum of the (average) resistance. However, for longer times diffusion tends to laterally spread the OV profiles, slightly increasing the resistivity values (see the subtle change in the color of the resistivity maps), the effective length of the CPs (see the right CP "bending" over to the left) and eventually merging the CPs. The combination of these effects redounds in an effective (but tiny) increase of the (average) resistance for  $\tau 2$  and  $\tau 3$ , respectively.

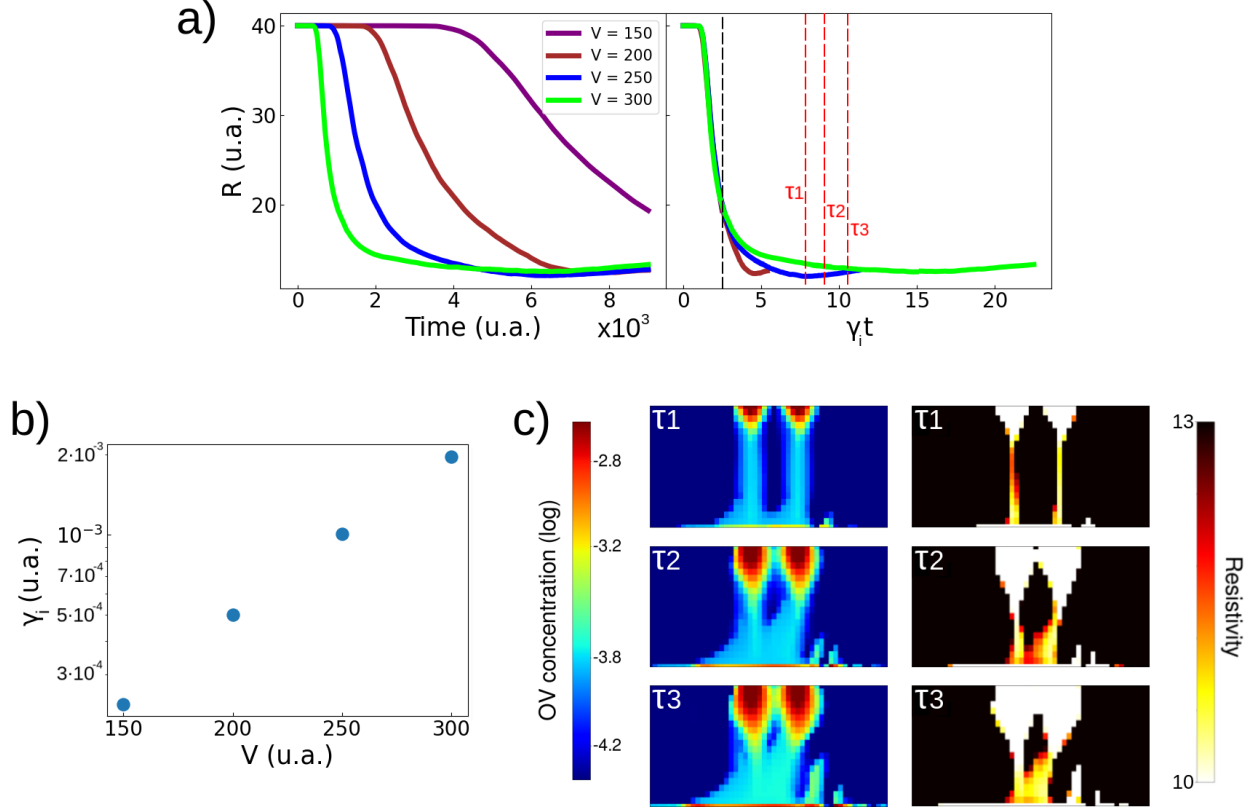


FIG. 4: a) Evolution of the resistance for four different applied voltages  $V_i = 150, 200, 250, 300$ , as a function of time (left) and as a function of  $\gamma_i t$ ,  $i = 1, 2, 3, 4$  (right). The collapse of the scaled curves is extremely good till  $\gamma_i t \sim 2$  (see the vertical dashed black line). Each curve is an average over nearly 100 realizations of the initial OV profile. b) log-lin plot of  $\gamma_i$  as a function of the applied voltages  $V_i$ ,  $i = 1, 2, 3, 4$ . c) Snapshots of the OV and resistivity profiles at times  $\tau k = \gamma_3 t k$ ,  $k = 1, 2, 3$  ( $\gamma_3 = 1 \cdot 10^{-3}$ ) indicated in Fig. 4 a) right panel. The profiles are for  $V_3 = 250$  a.u. and for a particular realization of the simulations. All simulations were carried out for  $v_O = 0$ .

Inspired by experimental protocols [9, 17], we can account for the RS effect applying a voltage ramp once the OVFs and CPs are formed. The results are plotted in Fig.5a) for a ramp with voltage  $V$  in the range  $-125 \leq V \leq 205$  a.u. The formed OVFs initially retract due to the applied negative stimulus and subsequently regrow during the positive ramp. Along a complete cycle, this retraction/regrowth gives rise to the RS effect, namely, the commutation of the resistance between two values, the high resistance (HR) and the low resistance (LR) state, respectively. This process is shown in Fig.5a) (top panel), for a single realization of the OV profile (blue line) and for an average over nearly a hundred of realizations (red dashed line). An overall well defined switching

is obtained. In addition, a “peak” in the resistance just before the SET (HR to LR) transition starts is clearly visible. This peak strongly resembles the “abnormal SET” analyzed by Park et al. in Ref. 17 and measured in TaO<sub>x</sub> and TiO<sub>x</sub>-based memristive devices [54, 55].

To dive into the origin of this peak, we focus on the evolution of the dominant CP for the positive ramp ( $V \geq 0$ ) (in the example we plot a single realization). The CP can be separated in two parts, named L1 and L2 (see Fig.5b) (left)) and thus the total resistance can be computed as the series resistance of both. In Fig.5a) (bottom panel) we show each resistance separately, noticing that while L1 resistance stays relatively constant, L2 resistance exhibits the peak observed for the total resistance in the top panel. To explain this behaviour we consider four times, labeled  $t1$  to  $t4$  (see top panel), and focus on the evolution of the OV and associated resistivity profiles of L2. The results are shown in Fig.5b). At time  $t1$ , most of the OV are concentrated in the upper part of L2, and the resistance is dominated by the bottom part of L2, where no OV are present and thus has an associated high resistivity. Afterwards, the positive applied voltage pushes the OVs downward and at time  $t2$  the OV that were formerly at the top part of L2 are spilled over the complete L2 section. In this situation, the resistance of the top part of L2 increases, while the OV density in the bottom part still remains below the threshold  $\delta_m$ , and no transition to  $L\rho$  takes place.

Therefore, this rearrange of OV on L2 increases the total resistance, and is at the origin of the peak obtained at  $t2$  before the SET. After this, OVs further migrate from L1 to L2 ( $t3$  and  $t4$ ) with the concomitant decrease of the resistance towards the LR state. It is important to note that, even when OVs migrate from L1 to L2, L1’s resistance remains stable due to its OV concentration is above the threshold needed for the transition to  $L\rho$ .

In summary the present analysis, entirely based in our model for OVF and CP formation, explains in a simple and direct way the anomalous peak experimentally detected in the SET transition of (at least) two of the most studied binary oxide-based memristors with FRS.

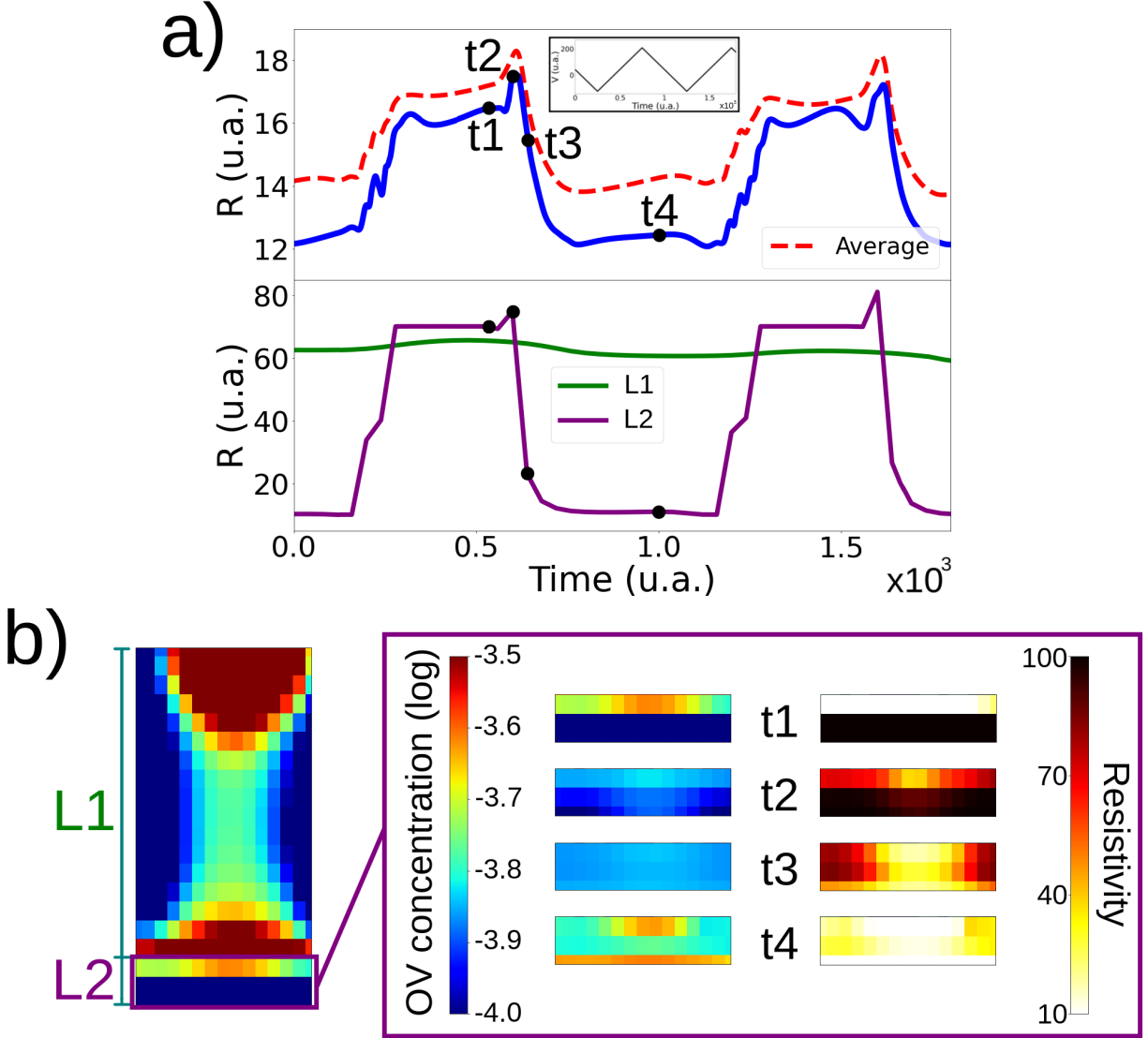


FIG. 5: a) Total resistance (top panel) and resistances of sections L1 and L2 of the dominant CP (bottom panel), as a function of time. Inset: applied voltage ramp. b) OVF and resistivity profiles along the section L2 of the dominant CP for times  $t_1$ ,  $t_2$ ,  $t_3$ ,  $t_4$  indicated in panel a).

### B. OVF and CP in the presence of static defects

Adding static defects significantly changes the OVF and CP formation dynamics, as we will discuss in the following. In Fig.6 we show OV profiles and the associated resistivities (bottom panels) for three values of the static defects density  $\nu_0 = 0.05, 0.15$  and  $0.5$ , respectively.

For  $\nu_0 = 0.05$  we identify in the AR three different structures for the OV configuration: The first one corresponds to OVF and CP connecting the TI and BI in a vertical line (the vertical magenta

line below the arrow ① is shown as a guide to the eye) similar to what we previously shown for  $\nu_0 = 0$  in Figs.2 and 3. The second one are OV that remain trapped due to the presence of static defects surrounding them (see the profile below the arrow ② as an example of this) and finally, "wiggle" OVF and CP that avoid the randomly distributed static defects (an example of this OV configuration is indicated by the magenta line plotted as a guide to the eye below ③).

Despite these different configurations, we notice that for this small concentration of static defects, an OVF is concomitant with the formation of a low resistivity CP, as can be seen in the lower panel of Fig.6 for  $\nu_0 = 0.05$ .

As the density of localized defects increases, another regime is obtained. For  $\nu_0 = 0.15$  for example, even though a percolating path reaching the BI is formed (see the magenta guiding line indicating an OVF formed through such a percolating path), the CP does not form, as is evident from the resistivity profiles displayed in the bottom panel. A sort of "granular" profile of resistivity is obtained: regions of lower resistivity, mainly near the TI and the BI, and regions of higher resistivity, mainly located in the middle of the AR. Therefore, an OVF can be formed in this regime, but its OV density is not enough to form a CP.

Finally, the third regime corresponds to higher densities  $\nu_0$  for which OV do not percolate, as exemplified by the  $\nu_0 = 0.5$  profile. In this regime all OV concentrate near the TI, and neither an OVF nor a CP is formed.

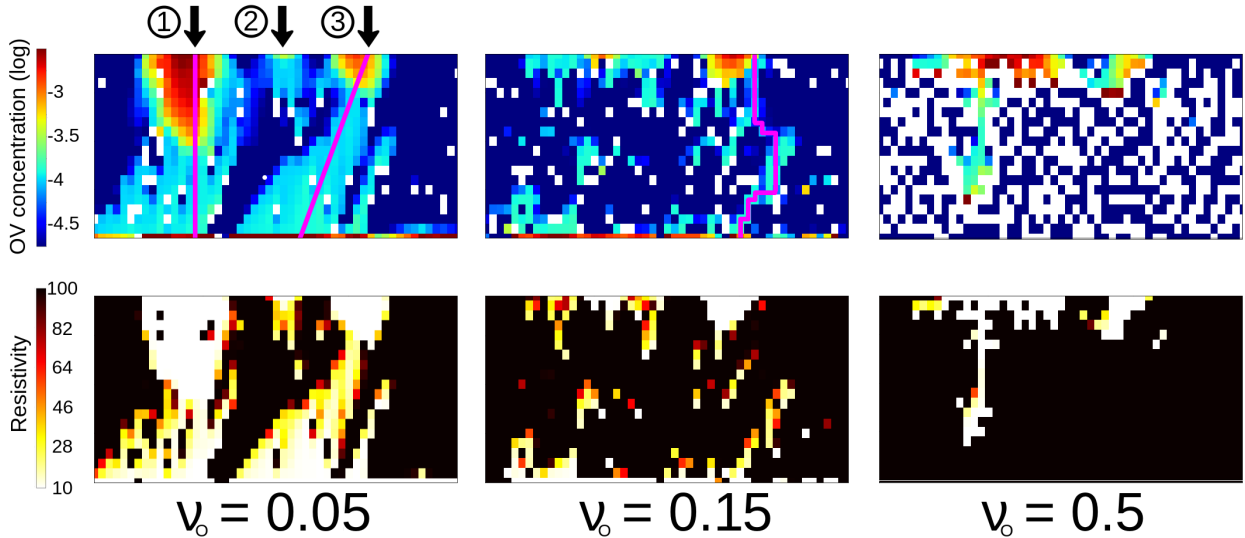


FIG. 6: OV (top panel) and resistivity (bottom panel) profiles for three static defect densities  $\nu_0 = 0.05$ ,  $0.15$  and  $0.5$ , taken once the profiles became stable in time. The magenta lines are guides to the eye.



From the precedent discussion it can be inferred that: i) the percolation of OV between the TI and BI is a prerequisite for the formation of an OVF, and ii) a CP can be formed only after an OVF is completed. Along this reasoning we carried out of the order of a hundred simulations for different static defects concentrations  $v_O$  to compute the percolation and CP formation probabilities. The percolation probability is defined in terms of the fraction of simulations in which there is a path through which OV can percolate from the TI to the BI. Analogously, the CP formation probability is defined as the fraction of simulations in which a CP is formed. It is important to note that we compute the CP probability once the resistivity and the OV profiles have stabilized.

From our analysis, we identify different thresholds for percolation and CP formation as a function of  $v_O$ . For  $v_O \sim 0$ , both the percolating path (P) and the CP are formed, as can be seen from Fig.7 (top and bottom panels). As  $v_O$  increases, we obtain a regime in which a percolating path is still formed (P) but the CP probability decreases. We named this region CPT (see the bottom panel of the Fig.7) and is defined for values of  $v_O$  in the interval  $(0.025, 0.15)$ . For larger values,  $0.15 < v_O \leq 0.3$ , the percolation probability remains equal to 1 in spite of the fact that the CP probability is negligible (we named this the NCP region). For  $0.3 < v_O < 0.6$  we define the PT region, in which the percolation probability decreases from 1 to 0. Finally after the PT region, for  $v_O \geq 0.6$ , neither the OV percolate (NP region) nor the CP are formed (NCP).

Theoretical works predict, in the thermodynamic limit, a threshold  $p_c = 0.59$  for the onsite percolation transition in square lattices [56, 57]. In our model, once we take into account that  $v_c \equiv 1 - p_c$  we can estimate a value of  $v_c \sim 0.45$ , which is in very good agreement with the theoretical prediction, considering that our system has a finite size.

An important remark is that the present results are robust and quite independent of the resistivity thresholds employed to define the CP, as can be seen in the three CP probability curves plotted in the bottom panel of Fig.7, which behave following the same trend. In addition, since lowering  $A$  in Eq.(1) could lead to different  $\delta_k$  values for each of the selected thresholds, we have checked that the limits of the CPT region remain roughly unchanged as the value of  $A$  is decreased in one order of magnitude.

The present analysis highlights the distinction between a percolating path and a CP. Even when OV percolate through the sample, this does not lead necessarily to a CP connecting top and bottom electrodes. Indeed, we obtained a whole range of  $v_O$  values where OV percolate without forming a CP but giving rise to the split profiles in the resistivity maps, as the one shown in Fig.6 for  $v_O = 0.15$ . In summary, OV percolation is a necessary but not a sufficient condition for the formation

of a CP.

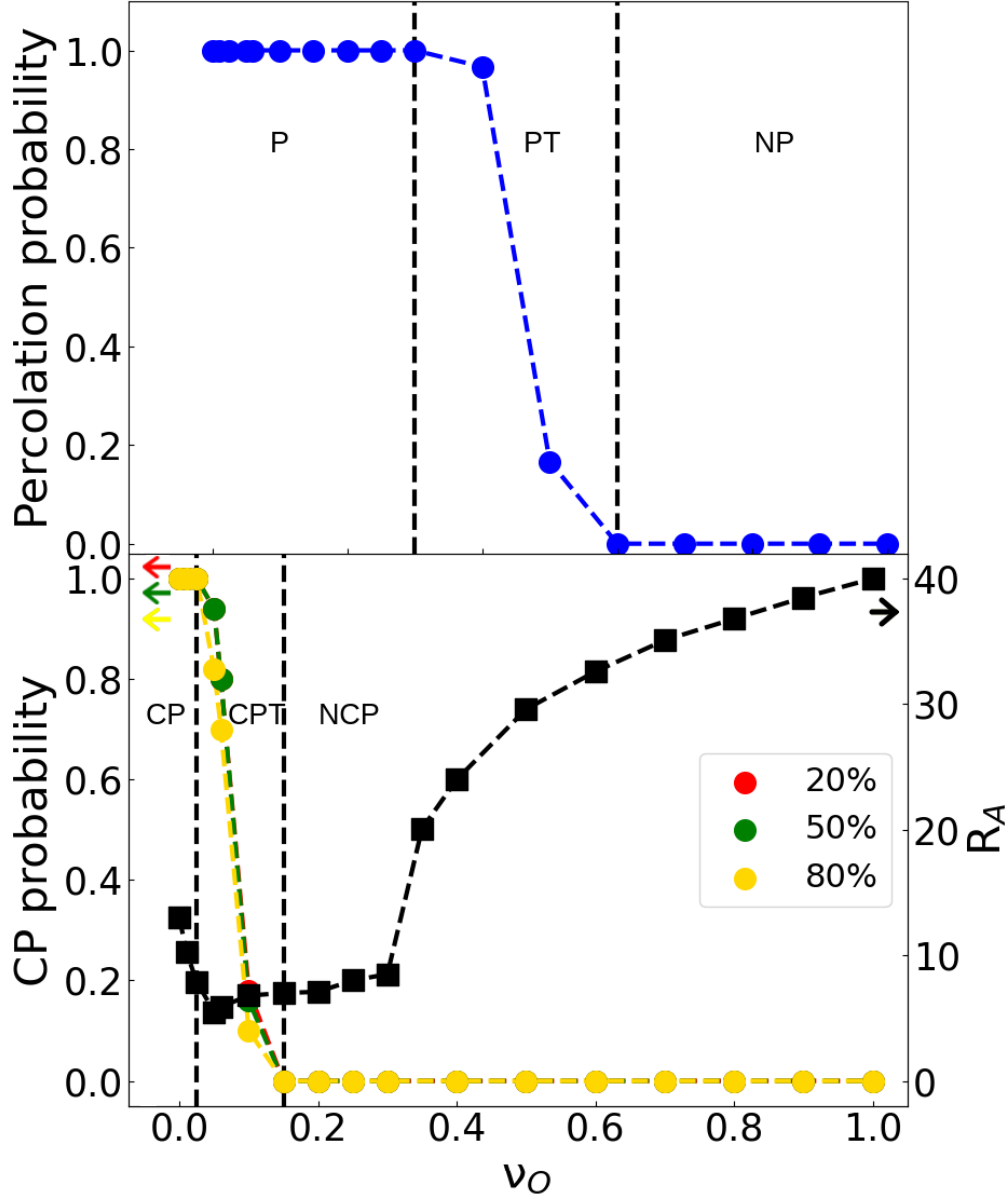


FIG. 7: Percolation probability (top panel), CP probability (bottom panel, left vertical axis) and asymptotic resistance  $R_A$  (bottom panel, right vertical axis) as a function of static defects concentration  $\nu_O$ . The CP probability is plotted for the three resistivity thresholds defined in Fig. 1 b). The dashed lines highlight the transition region between the different regimes described in the text (CP, CPT and NCP, respectively).

The resistance  $R(t)$  changes not only with the applied voltage, as we have already discussed in Sec.III A, but also with the concentration of static defects  $\nu_O$ . A small concentration of static defects is observed to reduce the asymptotic value of the resistance in comparison to the case  $\nu_O = 0$

(see for instance in Fig.8 a) the curve for  $v_O = 0.05$ ) -notice however that this occurs without a significant change of the time it takes for  $R(t)$  to stabilize . This rather paradoxical behavior is systematically observed for the smaller values of  $v_O$ - this is evident in the asymptotic resistance value,  $R_A$ , computed as a function of the defect concentration in the bottom panel of Fig.7, and it originates in the following. A small concentration of defects tends to disturb the movement of vacancies from TI to BI, producing fluctuations in their lateral concentration. These fluctuations promote further migration of vacancies through paths of high OV concentration, additionally reducing the resistance of these paths. In samples without defects there is no such a mechanism to promote the creation of localized low resistance paths. Of course this process can be active only for low enough defect concentration, that do not compromise the global conductivity of the sample. As the values of  $v_O$  further increase along the CPT region, OVF are still formed but several sites do not have the lowest resistivity and as a consequence the overall resistance  $R_A$  increases with  $v_O$ . However the competition between the average site resistivity and the number of OVFs results in a smooth increase of  $R_A$ . Finally, for values of  $v_O > 0.3$ , defects impede the formation of CPs (the CP probability is negligible) and a pronounced increase in the values of  $R_A$  is obtained.

These different responses impact on the temporal evolution of the resistance, as we discuss in the following. In Fig.8 a) we plot the resistance as a function of time for several values of  $v_O$  (the stimulus is  $V_3 = 250$  a.u. in all cases). The first observation is that as  $v_O$  increases the resistance drop starts earlier, as more defects in the top part of the AR causes OV to accumulate there with the concomitant transition in the lower resistivity values taken place earlier. This effect can be quantified in terms of the characteristic time  $\tau_{i,v_O}$  - defined as the time the resistance remains on its initial value for a voltage  $V_i = 150, 200, 250, 300$  ( $i = 1, 2, 3, 4$ ), and static defect density  $v_O$ : as  $v_O$  increases,  $\tau_{i,v_O}$  gets shorter. The vertical dashed lines in Fig.8 a) highlight this result for two characteristic times,  $\tau_{3,0}$  and  $\tau_{3,0.5}$ , respectively. In addition Fig. 8 b) shows  $\gamma_{3,v_O} \equiv 1/\tau_{3,v_O}$  (for  $V_3 = 250$  a.u ( $i = 3$ )) as a function of  $v_O$ . Despite the computed  $\gamma_{3,v_O}$  values exhibit a certain dispersion (that could be reduced with more statistics), a clear (and not linear) growth trend is obtained.

This analysis has been performed for other values of the applied voltages confirming that static defects modify the former scaling with voltage obtained for the case  $v_O = 0$  (and analyzed in Fig. 4). In Figure8 c) (left) we show three vertical panels, each one for a different value  $v_O = 0.05, 0.15, 0.5$  respectively, where the resistance is plotted as a function of time for the four different applied stimulus  $V_i = 150, 200, 250, 300$  ( $i = 1, 2, 3, 4$ ). On the right the scaled curves are

shown. The dashed vertical line in each plot shows the  $\gamma_{i,v_O}t$  at which the scaling is lost: As more static defects are added into the AR the scaling is lost earlier.

It is worth noting that our  $v_O$  parameter -related to the amount of blocking nodes present in our 2D resistor network- resembles the porosity  $\phi$ , defined in a material with voids as  $\phi = V_v / V_t$ , where  $V_v$  and  $V_t$  are the voids and total volume, respectively. We recall that the porosity in oxide thin films can reach values up to  $\phi \approx 0.25$  [58], strongly depending on the fabrication conditions, particularly the growth temperature ( $\Phi$  increases as the growth temperature decreases [59]). This shows that, if we assume  $\phi \approx v_0$ , the range of  $v_O$  in which we found the crossover from CP to CPT is well within the porosity range reported for oxides [58], highlighting the potential of our model to help determining the types of nanostructural features compatible with a robust filamentary memristive response.

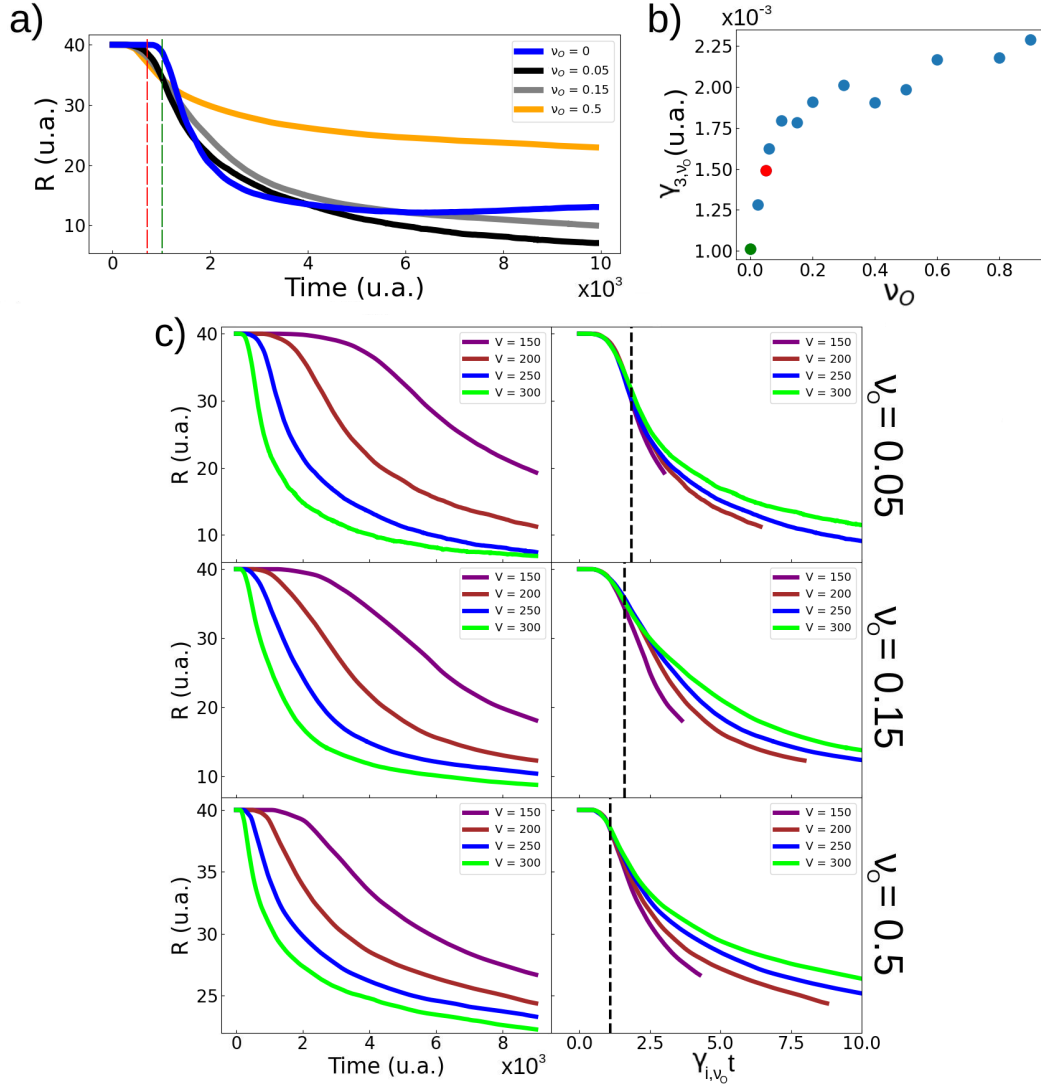


FIG. 8: a) Resistance as a function of time for four different  $v_O$  values and for applied stimulus  $V_3 = 250$  a.u. The vertical red and green dashed lines show two different characteristic times  $\tau_{3,0} = 1 \cdot 10^{-3}$  and  $\tau_{3,0.05} = 1.6 \cdot 10^{-3}$ , corresponding to  $v_O = 0, 0.05$  respectively. b)  $\gamma_{3,v_O} \equiv 1/\tau_{3,v_O}$  values as a function of the static defect density  $v_O$ . The voltage is  $V_3 = 250$  a.u. c) Resistance as function of time for  $v_O = 0.05, 0.15, 0.5$  (top, central and bottom panel) and for the four different applied voltages  $V_i$  (left panels). The scaled simulations are shown on the right. In each case the vertical dashed line indicates the scaled time above which the scaling is lost.

#### IV. CONCLUDING REMARKS

In this work, we analyze the growth and stability of OV filaments and low resistance conducting paths in memristive devices based on binary oxides, employing a 2d model which considers the dynamics of OV in a resistor network. We identify the main mechanisms involved in these processes noting that, even though a filament is formed, the OV concentration must exceed a critical value in all the sites in order to generate a low resistivity path. This finding unveils some additional complexity related to filament formation that, to the best of our knowledge, has not been previously addressed.

Our results describe, in addition, a filament formation dynamics that, preceding the transition to a low resistance state, involves the formation of multiple filaments with varying shape and lengths, leading finally to a "dominant filament" -the filament whose resistance follows qualitatively the overall device resistance. Our model also successfully recreates the RS effect when applying a voltage ramp, giving a simple explanation for an anomalous peak often seen before the SET transition in electrical measurements. The understanding of these features -all correlated with nanoscale OV dynamics- are essential to control the behavior of filamentary resistive switching devices.

The previous discussion shows that the OVRN model has the potential to further improve our understanding of TMO-based memristive system, noticing that it also helps determining the role of defects on the device electrical response. The inclusion of static defects -corresponding to voids in real (porous) materials- to our simulated system, further highlights the importance of the OVF/CP crossover in the electrical behavior, showing that there is a whole range of  $v_O$  values for which OVs percolate through the sample and OVFs are formed, but CPs are absent. This is of paramount importance to optimize the electrical behavior of devices, given the inverse correlation of thin layer porosity and fabrication temperature [58]. Our results allow determining the maximum porosity (correlated with a minimum growth temperature) that warrants the onset of conducting filaments. This is relevant for the development of CMOS-compatible devices, where thermal budget limitations critically constrain the fabrication process. In addition, we also show that the presence of static defects allows the achievement of lower low resistance states, enlarging in this way the device ON-OFF ratio, which is one of the key figures related to memristive devices design.

We also notice that our model can address the (un)stability of the filaments and conducting paths once the electrical stimulus is removed (volatile effect), which could be harnessed for the

development of neuron-like devices, an issue that will be addressed in a future work.

In summary, this paper aims to bridge the gap between theoretical modeling and experimental observations of filamentary resistive switching, offering a two-dimensional perspective that captures the complexities of defect dynamics and conductive filament formation. Our numerical study provides a more comprehensive understanding of filament evolution and its critical role in resistive switching, paving the way for the development and engineering of innovative memristive devices for in-memory or neuromorphic computing that integrate defects as part of their design [60].

**Acknowledgments** We acknowledge support from ANPCyT (PICT2019-02781, PICT2020A-00415, PICT2019-0564), UNCuyo (P06/C026-T1) and EU-H2020-RISE project MELON (Grant No. 872631).

## **AUTHOR DECLARATIONS**

### **Conflict of Interest**

The authors have no conflicts to disclose.

### **Data availability**

The data that support the findings of this study are available from the corresponding author upon reasonable request.

- 
- [1] S. Yu, *Neuro-inspired computing using resistive synaptic devices* (Springer International Publishing, 2017).
  - [2] M. Prezioso, F. Merrikh-Bayat, B. Hoskins, G. C. Adam, K. K. Likharev, and D. B. Strukov, Training and operation of an integrated neuromorphic network based on metal-oxide memristors, *Nature* **521**, 61 (2015).
  - [3] W. Zhang, B. Gao, J. Tang, P. Yao, S. Yu, M.-F. Chang, H.-J. Yoo, H. Qian, and H. Wu, Neuro-inspired computing chips, *Nature electronics* **3**, 371 (2020).
  - [4] J. D. Kendall and S. Kumar, The building blocks of a brain-inspired computer, *Applied Physics Reviews* **7** (2020).
  - [5] A. Sawa, Resistive switching in transition metal oxides, *Materials Today* **11**, 28 (2008).
  - [6] D. Ielmini and R. Waser, *Resistive Switching: From Fundamentals of Nanoionic Redox Processes to Memristive Device Applications* (Wiley-VCH, 2016).
  - [7] S. K. Nandi, S. K. Nath, A. E. El-Helou, S. Li, T. Ratcliff, M. Uenuma, P. E. Raad, and R. G. Elliman,

- Electric field- and current-induced electroforming modes in  $\text{nbo}_x$ , *ACS Appl. Mater. Interfaces* **12**, 8422 (2020).
- [8] N. Ghenzi, M. J. Sánchez, and P. Levy, A compact model for binary oxides-based memristive interfaces, *J. Phys. D: Appl. Phys.* **46**, 415101 (2013).
- [9] C. Ferreyra, M. Sánchez, M. Aguirre, C. Acha, S. Bengió, J. Lecourt, U. Lüders, and D. Rubi, Selective activation of memristive interfaces in  $\text{TaO}_x$ -based devices by controlling oxygen vacancies dynamics at the nanoscale, *Nanotechnology* **31**, 155204 (2020).
- [10] J. Y. Son and Y.-H. Shin, Direct observation of conducting filaments on resistive switching of NiO thin films, *Applied Physics Letters* **92**, 222106 (2008), [https://pubs.aip.org/aip/apl/article-pdf/doi/10.1063/1.2931087/13153362/222106\\_1\\_online.pdf](https://pubs.aip.org/aip/apl/article-pdf/doi/10.1063/1.2931087/13153362/222106_1_online.pdf).
- [11] V. Álvarez Martínez, R. Ramos, V. Leborán, A. Sarantopoulos, R. Dittmann, and F. Rivadulla, Interfacial thermal resistive switching in (pt,cr)/ $\text{srtio}_3$  devices, *ACS Applied Materials & Interfaces* **16**, 15043 (2024).
- [12] S. Wang, J. G. Ramírez, and I. K. Schuller, Avalanches in vanadium sesquioxide nanodevices, *Phys. Rev. B* **92**, 085150 (2015).
- [13] A. Sharoni, J. G. Ramírez, and I. K. Schuller, Multiple avalanches across the metal-insulator transition of vanadium oxide nanoscaled junctions, *Phys. Rev. Lett.* **101**, 026404 (2008).
- [14] J. Yang, M. Pickett, X. Li, D. Ohlberg, D. Stewart, and R. Williams, A fast, high-endurance and scalable nonvolatile memory device made from asymmetric  $\text{Ta}_2\text{O}_{5-x}/\text{TaO}_{2-x}$  bilayer structures, *Nat. Nanotechnol* **3**, 429 (2008).
- [15] M. Zhu, Z. Yu, G. Hu, K. Yu, Y. Jiang, J. Wang, W. Dong, J. Guo, Y. Qiu, G. Yu, and H.-M. Zhou, A  $\text{taox}/\text{tioy}$  bilayer memristor with enhanced synaptic features for neuromorphic computing, *Advanced Electronic Materials* **10**, 2400008 (2024).
- [16] T. Kim, H. Son, I. Kim, J. Kim, S. Lee, J. K. Park, J. Y. Kwak, J. Park, and Y. Jeong, Reversible switching mode change in  $\text{ta}_2\text{o}_5$ -based resistive switching memory (reram), *Scientific Reports* **10**, 11247 (2020).
- [17] T. H. Park, S. J. Song, H. J. Kim, S. G. Kim, S. Chung, B. Y. Kim, K. J. Lee, K. M. Kim, B. J. Choi, and C. S. Hwang, Thickness effect of ultra-thin  $\text{Ta}_2\text{O}_5$  resistance switching layer in 28 nm-diameter memory cell, *Scientific Reports* **5**, 15965 (2015).
- [18] J.-Y. Chen, C.-W. Huang, C.-H. Chiu, Y.-T. Huang, and W.-W. Wu, Switching kinetic of vcm-based memristor: evolution and positioning of nanofilament, *Advanced Materials* **27**, 5028 (2015).



- [19] K. Bao, J. Meng, J. D. Poplawsky, and M. Skowronski, Electrical conductivity of taox as function of composition and temperature, *Journal of Non-Crystalline Solids* **617**, 122495 (2023).
- [20] Y. Lu, Y. Matsuda, K. Sagara, L. Hao, T. Otomitsu, and H. Yoshida, Fabrication and thermoelectric properties of magnéli phases by adding ti into tio<sub>2</sub> (2012) pp. 1291–1296.
- [21] A. F. Arif, R. Balgis, T. Ogi, F. Iskandar, A. Kinoshita, K. Nakamura, and K. Okuyama, Highly conductive nano-sized magnéli phases titanium oxide (tiox), *Scientific Reports* **7**, 3646 (2017).
- [22] R. Waser and M. Aono, Nanoionics-based resistive switching memories, in *Nanoscience And Technology: A Collection of Reviews from Nature Journals* (World Scientific, 2010) pp. 158–165.
- [23] Y. C. Bae, A. R. Lee, J. B. Lee, J. H. Koo, K. C. Kwon, J. G. Park, H. S. Im, and J. P. Hong, Oxygen ion drift-induced complementary resistive switching in homo tiox/tioy/tiox and hetero tiox/tion/tiox triple multilayer frameworks, *Advanced functional materials* **22**, 709 (2012).
- [24] S. Balatti, S. Larentis, D. Gilmer, and D. Ielmini, Multiple memory states in resistive switching devices through controlled size and orientation of the conductive filament, *Advanced materials* **25**, 1474 (2013).
- [25] U. Celano, Y. Yin Chen, D. J. Wouters, G. Groeseneken, M. Jurczak, and W. Vandervorst, Filament observation in metal-oxide resistive switching devices, *Applied Physics Letters* **102**, 121602 (2013).
- [26] A. Isaev, O. Permyakova, and A. Rogozhin, Mechanisms of conductive filament formation in hafnium oxide multilayer structures, *Thin Solid Films* **781**, 139993 (2023).
- [27] D.-H. Kwon, K. M. Kim, J. H. Jang, J. M. Jeon, M. H. Lee, G. H. Kim, X.-S. Li, G.-S. Park, B. Lee, S. Han, *et al.*, Atomic structure of conducting nanofilaments in tio<sub>2</sub> resistive switching memory, *Nature nanotechnology* **5**, 148 (2010).
- [28] Y. Yang, P. Gao, S. Gaba, T. Chang, X. Pan, and W. Lu, Observation of conducting filament growth in nanoscale resistive memories, *Nature Communications* **3**, 732 (2012).
- [29] C.-N. Peng, C.-W. Wang, T.-C. Chan, W.-Y. Chang, Y.-C. Wang, H.-W. Tsai, W.-W. Wu, L.-J. Chen, and Y.-L. Chueh, Resistive switching of AU/ZnO/Au resistive memory: an in situ observation of conductive bridge formation, *Nanoscale research letters* **7**, 1 (2012).
- [30] K. Krishnan, T. Tsuruoka, C. Mannequin, and M. Aono, Mechanism for conducting filament growth in self-assembled polymer thin films for redox-based atomic switches, *Advanced Materials* **28**, 640 (2016).
- [31] S. Cheng, M.-H. Lee, X. Li, L. Fratino, F. Tesler, M.-G. Han, J. del Valle, R. C. Dynes, M. J. Rozenberg, I. K. Schuller, and Y. Zhu, Operando characterization of conductive filaments during resistive

- switching in mott vo2, Proceedings of the National Academy of Sciences **118**, e2013676118 (2021), <https://www.pnas.org/doi/pdf/10.1073/pnas.2013676118>.
- [32] G. Sassine, S. La Barbera, N. Najjari, M. Minvielle, C. Dubourdieu, and F. Alibart, Interfacial versus filamentary resistive switching in TiO<sub>2</sub> and HfO<sub>2</sub> devices, Journal of Vacuum Science & Technology B, Nanotechnology and Microelectronics: Materials, Processing, Measurement, and Phenomena **34**, 012202 (2016).
- [33] S. Brivio and S. Spiga, Stochastic circuit breaker network model for bipolar resistance switching memories, Journal of Computational Electronics **16**, 1154 (2017).
- [34] J. Xing, Q. Li, X. Tian, Z. Li, and H. Xu, A memristor random circuit breaker model accounting for stimulus thermal accumulation, IEICE Electronics Express **13**, 20160376 (2016).
- [35] A. Roy and P.-R. Cha, Electric field induced charge migration and formation of conducting filament during resistive switching in electrochemical metallization (ECM) memory cells, Journal of Applied Physics **128**, 205102 (2020), [https://pubs.aip.org/aip/jap/article-pdf/doi/10.1063/5.0026350/14816820/205102\\_1\\_online.pdf](https://pubs.aip.org/aip/jap/article-pdf/doi/10.1063/5.0026350/14816820/205102_1_online.pdf).
- [36] D. Maldonado, A. Cantudo, F. M. Gómez-Campos, Y. Yuan, Y. Shen, W. Zheng, M. Lanza, and J. B. Roldán, 3d simulation of conductive nanofilaments in multilayer h-bn memristors via a circuit breaker approach, Mater. Horiz. **11**, 949 (2024).
- [37] P. Xu, W. Fa, and S. Chen, Computational study on filament growth dynamics in microstructure-controlled storage media of resistive switching memories, ACS Nano **17**, 10511 (2023), <https://doi.org/10.1021/acsnano.3c01405>.
- [38] M. J. Rozenberg, M. J. Sánchez, R. Weht, C. Acha, F. Gomez-Marlasca, and P. Levy, Mechanism for bipolar resistive switching in transition-metal oxides, Phys. Rev. B **81**, 115101 (2010).
- [39] R. L. Martir, M. J. Sánchez, M. Aguirre, W. Quiñonez, C. Ferreyra, C. Acha, J. Lecourt, U. Lüders, and D. Rubi, Oxygen vacancy dynamics in pt/tiox/taoy/pt memristors: exchange with the environment and internal electromigration, Nanotechnology **34**, 095202 (2022).
- [40] K. Bejtka, G. Milano, C. Ricciardi, C. F. Pirri, and S. Porro, Tem nanostructural investigation of Ag-conductive filaments in polycrystalline ZnO-based resistive switching devices, ACS Appl. Mater. Interfaces **12**, 29451 (2020).
- [41] H. Clarke, T. Brown, J. Hu, R. Ganguli, A. Reed, A. Voevodin, and P. J. Shamberger, Microstructure dependent filament forming kinetics in HfO<sub>2</sub> programmable metallization cells, Nanotechnology **27**, 425709 (2016).

- [42] X. Yan, Y. Li, J. Zhao, Y. Li, G. Bai, and S. Zhu, Roles of grain boundary and oxygen vacancies in Ba<sub>0.6</sub>Sr<sub>0.4</sub>TiO<sub>3</sub> films for resistive switching device application, *Applied Physics Letters* **108**, 033108 (2016).
- [43] B. Chakrabarti, H. Chan, K. Alam, A. Koneru, T. E. Gage, L. E. Ocola, R. Divan, D. Rosenmann, A. Khanna, B. Grisafe, T. Sanders, S. Datta, I. Arslan, S. K. R. S. Sankaranarayan, and S. Guha, Nanoporous Dielectric Resistive Memories Using Sequential Infiltration Synthesis, *ACS Nano* **15**, 4155 (2021).
- [44] J. J. Bucki and K. J. Kurzydłowski, Analysis of the effect of grain size uniformity on the flow stress of polycrystals: Part i: Studies of the relationship between the variance of grain volume and the variance of the grain area on polycrystal cross section, *Materials Characterization* **29**, 365 (1992).
- [45] J. Lee, W. Schell, X. Zhu, E. Kioupakis, and W. D. Lu, Charge transition of oxygen vacancies during resistive switching in oxide-based rram, *ACS Appl. Mater. Interfaces* **11**, 11579 (2019).
- [46] Y. Ma, D. Li, A. A. Herzing, D. A. Cullen, B. T. Sneed, K. L. More, N. T. Nuhfer, J. A. Bain, and M. Skowronski, Formation of the conducting filament in taox-resistive switching devices by thermal-gradient-induced cation accumulation, *ACS Applied Materials & Interfaces* **10**, 23187 (2018), pMID: 29912544, <https://doi.org/10.1021/acsami.8b03726>.
- [47] S. Dirkmann, M. Ziegler, M. Hansen, H. Kohlstedt, J. Trieschmann, and T. Mussenbrock, Kinetic simulation of filament growth dynamics in memristive electrochemical metallization devices, *Journal of Applied Physics* **118**, 214501 (2015).
- [48] G. Milano, M. Luebben, M. Laurenti, L. Boarino, C. Ricciardi, and I. Valov, Structure-dependent influence of moisture on resistive switching behavior of zno thin films, *Advanced Materials Interfaces* **8**, 2100915 (2021), <https://onlinelibrary.wiley.com/doi/pdf/10.1002/admi.202100915>.
- [49] S. Menzel, P. Kaupmann, and R. Waser, Understanding filamentary growth in electrochemical metallization memory cells using kinetic monte carlo simulations, *Nanoscale* **7**, 12673 (2015).
- [50] W. Wang, E. Covi, Y.-H. Lin, E. Ambrosi, A. Milozzi, C. Sbandati, M. Farronato, and D. Ielmini, Switching dynamics of ag-based filamentary volatile resistive switching devices—part ii: Mechanism and modeling, *IEEE Transactions on Electron Devices* **68**, 4342 (2021).
- [51] G. Milano, G. Pedretti, K. Montano, S. Ricci, S. Hashemkhani, L. Boarino, D. Ielmini, and C. Ricciardi, In materia reservoir computing with a fully memristive architecture based on self-organizing nanowire networks, *Nature Materials* **21**, 195 (2022).
- [52] S. La Barbera, D. Vuillaume, and F. Alibart, Filamentary Switching: Synaptic Plasticity through De-

- vice Volatility, ACS Nano **9**, 941 (2015).
- [53] S. Tang, F. Tesler, F. G. Marlasca, P. Levy, V. Dobrosavljević, and M. Rozenberg, Shock waves and commutation speed of memristors, Phys. Rev. X **6**, 011028 (2016).
- [54] H. Zhang, Y. Sijung, S. Menzel, C. F. W. D. J. H. C. S. W. R. Funck, Carsten, and S. Hoffmann-Eifert, Understanding the coexistence of two bipolar resistive switching modes with opposite polarity in Pt/TiO<sub>2</sub>/Ti/Pt nanosized reram devices, ACS Applied Materials and Interfaces **10**, 29766 (2018).
- [55] T. H. Park, H. J. Kim, W. Y. Park, S. G. Kim, B. J. Choi, and C. S. Hwang, Roles of conducting filament and non-filament regions in the ta2o5 and hfo2 resistive switching memory for switching reliability, Nanoscale **9**, 6010 (2017).
- [56] M. E. J. Newman and R. M. Ziff, Efficient monte carlo algorithm and high-precision results for percolation, Phys. Rev. Lett. **85**, 4104 (2000).
- [57] S. Mertens, Exact site-percolation probability on the square lattice, Journal of Physics A: Mathematical and Theoretical **55**, 334002 (2022).
- [58] S. Bagga, J. Akhtar, and S. Mishra, Influence of porosity on the properties of nanostructured tin oxide thin film, Materials Research Express **5**, 116406 (2018).
- [59] R. W. Smith and D. J. Srolovitz, Void formation during film growth: A molecular dynamics simulation study, Journal of Applied Physics **79**, 1448 (1996), [https://pubs.aip.org/aip/jap/article-pdf/79/3/1448/18681037/1448\\_1\\_online.pdf](https://pubs.aip.org/aip/jap/article-pdf/79/3/1448/18681037/1448_1_online.pdf).
- [60] W. Banerjee, Q. Liu, and H. Hwang, Engineering of defects in resistive random access memory devices, Journal of Applied Physics **127**, 051101 (2020), [https://pubs.aip.org/aip/jap/article-pdf/doi/10.1063/1.5136264/19892156/051101\\_1\\_1.5136264.pdf](https://pubs.aip.org/aip/jap/article-pdf/doi/10.1063/1.5136264/19892156/051101_1_1.5136264.pdf).